Shot noise in Aharonov-Bohm interferometer based on helical edge states

© R.A. Niyazov[1,2], I.V. Krainov[1], D.N. Aristov[1,2,3], V.Y. Kachorovskii[1]

[1] Ioffe Institute,
194021 St. Petersburg, Russia
[2] Petersburg Nuclear Physics Institute named by B.P. Konstantinov of NRC „Kurchatov Institute“,
188300 Gatchina, Russia
[3] Department of Physics, St. Petersburg State University,
199034 St. Petersburg Russia

E-mail: niyazov_ra@pnpi.nrcki.ru

Received October 15, 2025
Revised October 29, 2025
Accepted November 6, 2025

Shot noise in Aharoanov–Bohm interferometers formed by helical edge states of two-dimensional topological insulators has been investigated. The study demonstrates that noise measurements provide unique opportunities for studying the breakdown of topological protection. Unlike conventional interferometers, where interference occurs in the ballistic regime, the manifestation of interference effects in helical systems requires the presence of defects leading to backscattering. A key finding is that the Fano factor exhibits oscillations with a magnetic flux period of $\Delta\phi = 1/2$, where the oscillation amplitude is directly proportional to the backscattering strength. Furthermore, it is shown that simultaneous measurement of conductance and noise enables direct determination of the backscattering probability without detailed knowledge of contact properties. This provides a crucial experimental tool for identifying and quantifying the mechanisms responsible for the breakdown of topological protection in real materials. The results are particularly relevant for recent experiments with quantum point contacts on helical edge states and propose a noise spectroscopy method for characterizing topological phases. We also compare our results with the case of a conventional spinless single-channel interferometer.

Keywords: Helical edge states, Topological insulators, Shot noise, Aharonov–Bohm effect, Topological protection.

DOI: 10.61011/SC.2025.08.62602.8665

1. Introduction

Two-dimensional topological insulators (2D TIs) represent a novel phase of quantum matter characterized by an insulating bulk and conducting helical edge states [1–3]. These edge states exhibit remarkable properties: they are topologically protected against backscattering from nonmagnetic impurities and conduct current without dissipation. The helical nature — where electron spin is locked to propagation direction — makes these systems promising candidates for spintronic applications and topological quantum computing.

A fundamental question in the study of 2D TIs concerns the robustness of topological protection in real materials. While ideal helical edge states should exhibit perfect conductance quantization, experimental realizations often show significant deviations [4], suggesting the presence of backscattering mechanisms that violate topological protection. Identifying and characterizing these mechanisms remains an important challenge.

In this context, helical interferometers (HI), i. e. interferometric setups based on helical edge states (see Figure 1) provide a powerful probe of edge state properties. When arranged in the geometry of a ring enclosing a magnetic flux, these systems become sensitive to phase-coherent processes that can reveal the presence and nature of backscattering centers.

Here, we present a comprehensive theoretical study of shot noise in HI. Shot noise originates from the discrete nature of electric charge and provides complementary information to conductance measurements. Unlike conductance, which depends only on the average transmission, noise spectroscopy reveals fundamental properties of charge carriers — including their effective charge and quantum statistics — as well as characteristic energy scales of the system [5,6]. We characterize this noise through the Fano factor $\mathscr{F}$, defined as the ratio of the actual shot noise power to the classical Schottky value $2eI$. This dimensionless quantity serves as a key indicator of transport regimes: for instance, the universal values $\mathscr{F} = 1/3$ for diffusive conductors and $\mathscr{F} = 1/2$ for tunneling through a single quantum level reflect fundamental statistical properties independent of microscopic details.

It is worth noting that the shot noise in helical edge states (HES) has already been discussed for the case of infinite edge [7–18], i. e. without taking into account the interference effects. In particular, a great attention was paid to infinite HES with a dynamic magnetic impurity [11,13–17], whose magnetic moment changes direction after each scattering event. Discussing HI in this paper, we focus on the opposite case of static backscattering defect, which is not necessarily

magnetic (in particular, backscattering mechanisms involving charged puddles in the bulk of topological insulator are actively discussed [19]). We will describe such defect by S-matrix of general type. The experimental measurement of the Fano factor of HI at zero magnetic field for the edge states of 2D TI gives the value $0.1 < \mathscr{F} < 0.3$ [9,12]. The upper value, 0.3, is close to the value $1/3$ for diffusive conductor. A similar result was obtained in the model with a large number of „islands", allowing spin relaxation and tunnel-connected to the HES [20]. The effect of islands of different types on HES is currently being actively debated (see also recent works [4,21] and references therein).

At weak tunnel coupling and low temperatures, the conductance $G(\phi)$ displays sharp resonances at specific magnetic flux values due to the Aharonov–Bohm (AB) effect [22,23], occurring when quantum levels align with the Fermi energy [24,25]. Here ϕ is dimensionless magnetic flux $\phi = \Phi/\Phi_0$ threading the device, where $\Phi_0 = hc/e$ is the flux quantum and $\Phi = BS$, where B is homogeneous magnetic field and S is the area of the region encompassed by one-dimensional helical channel.

The high-temperature regime $T \gg \Delta$, where $\Delta = 2\pi v_F/L$ is the level spacing ($L = L_1 + L_2$ being the total interferometer length), reveals more subtle interference phenomena. While one might expect thermal averaging to suppress quantum interference, several theoretical works have demonstrated that both conventional [26–31] and helical [32–35] interferometers exhibit robust conductance oscillations even when $T \gg \Delta$. Remarkably, in this regime the resonances transform into narrow antiresonances — sharp conductance dips that persist despite thermal broadening. These antiresonances originate from energy-independent destructive interference between specific electron trajectories that remain coherent across the thermal window.

For conventional interferometers, the high-temperature conductance has been extensively studied, including effects of electron-electron interactions [27], disorder [29], and spin-orbit coupling [28]. More recently, these investigations have been extended to helical systems, examining single rings with static magnetic defects [32–35] and arrays of coupled helical rings [36]. Other interferometer geometries have also been explored [37–39].

Surprisingly, despite extensive literature on both systems, shot noise in the high-temperature regime $T \gg \Delta$ remained largely unexplored non only for helical but even for conventional interferometers. Previous noise studies focused primarily on the low-temperature limit $T \ll \Delta$: see Ref. [40] for conventional interferometers and Refs. [41,42] for helical systems. This gap is particularly notable given that noise measurements provide complementary information to conductance, potentially revealing distinct signatures of quantum interference in conventional versus topological systems.

The development of a comprehensive noise theory for both conventional and helical interferometers is timely given recent experimental advances. Conventional nanoscale rings with few conducting channels have been realized for over two decades [43–47], while recent experiments have demonstrated quantum point contacts to helical edge states [48], enabling detailed interferometric studies. The condition $T \gg \Delta$ is experimentally accessible — for typical Fermi velocities $v_F \sim 10^7$ cm/s and micron-scale devices, Δ corresponds to temperatures of just a few Kelvin, allowing interference effects to be studied at practically relevant temperatures.

For helical interferometers, magnetic fields introduce competing effects: they generate the AB phase necessary for interference while potentially decreasing topological protection due to the Zeeman effect. Crucially, the flux quantum $\Phi_0 = hc/e$ corresponds to fields of only ~ 3 Oe for micron-scale devices, well below the threshold where topological protection is significantly suppressed [49–51]. This separation of scales enables clean observation of AB oscillations in helical systems without destroying their topological character.

Recently we discussed shot noise both in helical [52] and conventional [53] interferometers. As for helical case, we considered HI with identical contacts and calculated the noise power in the high-T regime paying attention to the interference effects. We found the Fano factor strongly depending on the tunneling coupling and strength of backscattering defect.

Here, we further develop the results obtained in Ref. [52]. We present a detailed study of the sharp Aharonov–Bohm peaks in the Fano factor of the noise. Our key finding is that noise measurements provide unique information about backscattering defects that is inaccessible through conductance alone. Specifically, we demonstrate that the simultaneous measurement of conductance and Fano factor allows direct determination of the backscattering strength, independent of detailed knowledge about the contacts. Moreover, we show that the amplitude of AB oscillations in the Fano factor is directly proportional to the backscattering probability, offering a quantitative measure of topological protection breakdown. Having also in mind the recent experiment [48], we generalize here the calculation of the Fano factor of HI for experimentally relevant case of non-equivalent contacts. Also, at the Sec. 4 we will make a comparison with a conventional spinless single-channel interferometer (SCI) discussed recently in our work Ref. [53].

2. Model

We calculate current shot noise in mesoscopic interferometer where the conducting paths are formed by helical edge states of two-dimensional topological insulators, as depicted in Figure 1. In our model, the Fermi level resides within the bulk band gap, ensuring that transport occurs exclusively through the topologically protected edge channels. The connection to external measurement circuits is described using conventional spinful single-channel wires,

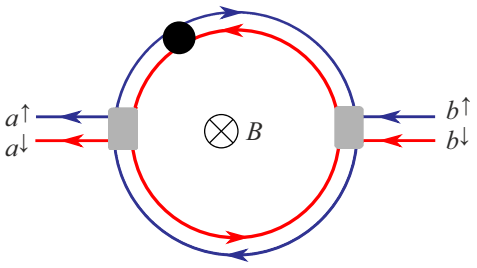

Figure 1. Aharonov–Bohm interferometers based on helical edge channels of 2D topological insulator. The leads (shown by gray color) are modeled by conventional single-channel and spinful wires. The black dot represents a backscattering impurity. Gray regions represent contacts described by 4×4 S-matrix [see Eq. (1) and Figure 2]. Homogeneous magnetic field, B, is perpendicular to the picture plane. Corresponding magnetic flux, $\Phi = BS$, is proportional to the area, S, of the region encompassed by one-dimensional channels.

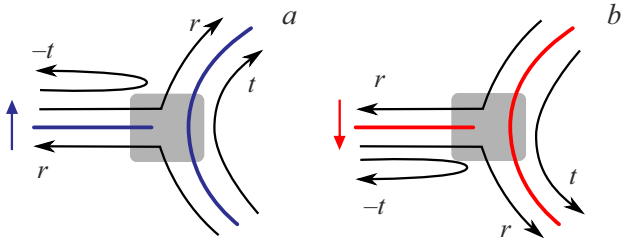

Figure 2. The scattering amplitudes entering scattering matrix of contacts, Eq. (1), which are modeled as a single-channel spinful wire. It is assumed that there is no spin flip at the contact and the two spin polarizations at the contact (shown by red and blue color) are completely separated. The $t \to 1$ case corresponds to a tunnel contact, and the $t \to 0$ case models a metal contact. Contact region with area S_0 is shown by gray color. We assume that $BS_0 \ll \Phi_0$, so that the field does not affect S-matrix.

establishing a framework that bridges the topological system with standard mesoscopic probes.

The simplest scattering matrix of a non-magnetic lead has the form

$$\hat{S} = \begin{pmatrix} -t & r & 0 & 0 \\ r & t & 0 & 0 \\ 0 & 0 & -t & r \\ 0 & 0 & r & t \end{pmatrix}, \quad t^2 + r^2 = 1, \tag{1}$$

where two identical blocks are responsible for two spins, and the basis is chosen in accordance with the spin polarization of the helical states at the point of contact (red and blue in Figure 2. It is convenient to parameterize amplitudes t and r by a parameter λ:

$$t = e^{-\lambda}, \quad r = \sqrt{1 - e^{-2\lambda}}, \quad 0 < \lambda < \infty. \tag{2}$$

Due to the topological protection, backscattering appears in the HI only in presence of a defect that violate time-reversal symmetry, in particular, in presence of magnetic defects or in case of magnetization of the leads. We assume in this paper that the leads are non-magnetic, but there is a static backscattering defect in one of the arms of the interferometer. As we already mentioned, much attention was drawn recently to the infinite HES with a dynamic magnetic impurity [11,13–17]), whose magnetic moment changes direction after each scattering event. For the isotropic exchange interaction between the impurity and the HES, the impurity's magnetic moment relaxes within the so-called Korringa time towards the local direction of the electron spin in the HES and, as a consequence, the interaction between the impurity and the HES becomes completely ineffective (see discussion in [11]). Accordingly, the problem of the noise intensity at zero frequency in the HES with a single impurity makes sense only in the presence of an anisotropic exchange interaction [13] (or an external magnetic field acting on a dynamic impurity [17]), while in the limit of isotropic exchange interaction Fano factor is singular [13], i. e. the result for the $\mathscr{F}$ depends on the order in which the constants responsible for the anisotropy tend to zero (see also discussion in [54]).

At the same time, the relaxation of the impurity's magnetic moment in reality stems not only from the interaction with the HES, but also from the environment of the impurity, which should provide a non-singular response for the $\mathscr{F}$ even for the isotropic exchange interaction. Therefore, it seems no less interesting to study the case which is opposite to one considered in the papers [11,13–17], namely, the case of a static magnetic defect with a large spin, which is robustly connected to the external environment.

Such a defect ensures the existence of a magnetic field in a small region of the HES, i. e. it allows elastic backward scattering without tunneling coupling between the HES and defect. Possible experimental realization is, for example, a potential dielectric ferromagnetic point contact with high magnetic stiffness and with the magnetic moment, whose direction is determined by uniaxial anisotropy and the demagnetization tensor of the ferromagnet. The possibility of creating static magnetic contacts to the HES has also been discussed [55].

Importantly, backscattering can occur not only due to magnetic defect but also due to the interaction with a charged puddle in the bulk of the topological insulator [19] or due to a point-like non-magnetic scatterer, with account for the electron-electron interaction [56].

Here, we assume the presence of static backscattering defect (BD) at the edge of the TI, which is described by the scattering matrix of the most general type

$$\hat{S}_{\mathrm{BD}} = \begin{pmatrix} \cos\theta\ e^{i\alpha} & i\sin\theta\ e^{i\varphi} \\ i\sin\theta\ e^{-i\varphi} & \cos\theta\ e^{-i\alpha} \end{pmatrix}. \tag{3}$$

For the case of magnetic defect, we neglect the back influence of the HES on the parameters of S_{BD}. The backward scattering rate, $R_\theta = \sin^2\theta$, is determined by the quantity θ while the phase φ has the meaning of the backward scattering phase on the BD.

Here we derive analytical expressions for a single BD placed in the upper shoulder. We consider interferometer with the lengths of the upper and lower shoulders given by L_1 and L_2, respectively. The BD is placed at position x_0 such that $0 < x_0 < L_1$. Using expression for scattering matrix (**??**), one can easily find transfer matrix of the defect

$$\hat{T}_{\rm BD} = \frac{e^{-i\alpha}}{\cos\theta}\begin{pmatrix} 1 & i\sin\theta\ e^{-i\xi} \\ -i\sin\theta\ e^{i\xi} & 1 \end{pmatrix}, \qquad (4)$$

where $\xi = \varphi - 2kx_0$ and $k = \varepsilon/v_F$ is the electron wave vector. One can show that the forward scattering phase α can be fully incorporated into the shift of ϕ, so that we put $\alpha = 0$ below.

3. Shot noise and conductance

3.1. General equations

In this Section, we calculate $\mathscr{F}$ assuming that a fixed bias voltage V is applied to leads. (In this paper, we assume that the external impedance is zero and therefore the voltage does not fluctuate. For a finite impedance both current and voltage fluctuate as discussed in detail in Ref. [6].) We will consider the most interesting and easily realized case:

$$\Delta \ll T \ll eV. \qquad (5)$$

The current noise is related with fluctuations of the electric current with respect to its average value $\delta\hat{I}(t) = \hat{I}(t) - \langle\hat{I}\rangle$. Here $\hat{I}$ is the current operator (an analytical expression for $\hat{I}$ is given in [5,6]).

The current correlation function associated with the noise is defined by:

$$\mathcal{S}(t-t') = \frac{1}{2}\langle\delta\hat{I}(t)\delta\hat{I}(t') + \delta\hat{I}(t')\delta\hat{I}(t)\rangle.$$

The Fourier transform of $\mathcal{S}$ gives an expression for the noise power: $S(\omega) = 2\int_{-\infty}^{\infty} dt\, e^{i\omega t}S(t)$ [the factor 2 in this expression is a matter of convention, see Eq. (1) in Ref. [5] and the comment after Eq (49) in Ref. [6]].

Spin-dependent transport through the two-terminal device is fully characterized by the matrix of energy-dependent transmission amplitudes $\hat{t} = t_{\alpha\beta}(\varepsilon)$ (here α and β are the spin indices associated with the outgoing and the incoming electrons, respectively) [5,6]:

$$\mathcal{S}(\omega=0) = 2G_0\int_{\mu}^{\mu+eV} d\varepsilon\,{\rm Tr}\left[\hat{\mathscr{T}}(\varepsilon)\left(1-\hat{\mathscr{T}}(\varepsilon)\right)\right], \qquad (6)$$

where $G_0 = e^2/h$ conductance quantum and

$$\hat{\mathscr{T}}(\varepsilon) = \hat{t}(\varepsilon)\hat{t}^{\dagger}(\varepsilon). \qquad (7)$$

The averaged current, $I = \langle\hat{I}\rangle$, and the Fano factor are given by

$$eI = G_0\int_{\mu}^{\mu+eV} d\varepsilon\,{\rm Tr}\left[\hat{\mathscr{T}}(\varepsilon)\right], \qquad (8)$$

$$\mathscr{F} = \frac{\mathcal{S}(\omega=0)}{2eI} = \frac{\int_{\mu}^{\mu+eV} d\varepsilon\,{\rm Tr}\left[\hat{\mathscr{T}}(1-\hat{\mathscr{T}})\right]}{\int_{\mu}^{\mu+eV} d\varepsilon\,{\rm Tr}[\hat{\mathscr{T}}]}. \qquad (9)$$

The transmission amplitudes $t_{\alpha\beta}(\varepsilon)$ varies on an energy scale on the order of the level spacing. We focus on the case, when the conditions (5) are satisfied. Then for the $\mathscr{F}$ we have

$$\mathscr{F} = \frac{{\rm Tr}\langle\hat{\mathscr{T}}(1-\hat{\mathscr{T}})\rangle_{\varepsilon}}{{\rm Tr}\langle\hat{\mathscr{T}}\rangle_{\varepsilon}}. \qquad (10)$$

where the averaging is taken over a temperature window in the vicinity of the Fermi level in the limit $T \gg \Delta$. Having in mind that spectrum of the helical states is linear, $\varepsilon = v_F k$, we find that the energy averaging is reduced to calculation of the integral $\langle\cdots\rangle_{\varepsilon} = \Delta^{-1}\int_0^{\Delta} d\varepsilon\,(\cdots) = \frac{L}{2\pi}\int_0^{2\pi/L} dk\,(\cdots)$ (see details in Ref. [53], App. A).

As seen from (8), the conductance is proportional to the transmission coefficient averaged over the spin and the energy:

$$\mathscr{T} = {\rm Tr}\langle\hat{\mathscr{T}}\rangle_{\varepsilon}/2 \qquad (11)$$

Introducing also the average

$$\mathscr{T}_2 = {\rm Tr}\langle\hat{\mathscr{T}}\hat{\mathscr{T}}\rangle_{\varepsilon}, \qquad (12)$$

one can write the Fano factor in the following form:

$$\mathscr{F} = 1 - \frac{\mathscr{T}_2}{2\mathscr{T}}, \qquad (13)$$

In the next section we will discuss calculations that allow one to find $\mathscr{F}$, using Eq. (13). Technically, the key idea is to present the matrix of transmission amplitudes in a special form, which allows performing the energy averaging analytically.

3.2. Transmission amplitude

Next, we discuss the Fano factor of the current noise in HI having two arms with lengths L_1 and L_2. We start with formula for energy dependent amplitude $\hat{t}(\varepsilon)$, which is a matrix in spinful case, and then perform energy averaging. The analytical expression obtained for $\mathscr{F}$ is rather cumbersome, so we present it in the Appendices A (for identical contacts) and-B (for non-dentical contacts) focusing in the main text on the most interesting limiting cases.

The matrix of the transmission amplitudes $\hat{t}$ from one contact to another is defined as follows

$$\begin{pmatrix} a^{\uparrow} \\ a^{\downarrow} \end{pmatrix} = \hat{t}\begin{pmatrix} b^{\uparrow} \\ b^{\downarrow} \end{pmatrix}, \qquad (14)$$

where $(b^{\uparrow}, b^{\downarrow})$ and $(a^{\uparrow}, a^{\downarrow})$ are the amplitudes of incoming (from the right contact) and outgoing (to the left contact) waves, respectively (see Figure 1). This matrix has been obtained earlier [33]:

$$\hat{t} = \frac{r^2 e^{2\pi i\phi L_1/L}}{t^2}\begin{pmatrix} e^{ikL_1} & 0 \\ 0 & e^{-ikL_1} \end{pmatrix}\begin{pmatrix} t & 0 \\ 0 & 1 \end{pmatrix}\hat{g}\begin{pmatrix} t & 0 \\ 0 & 1 \end{pmatrix},$$

$$\hat{g} = \cos\theta\left[\begin{pmatrix} 0 & 0 \\ 0 & -1 \end{pmatrix} + \frac{1}{2}\sum_{\alpha=\pm1}\frac{1+\alpha\hat{H}}{1-t^2e^{i(kL+\alpha 2\pi\phi_0)}}\right]. \qquad (15)$$

Here, t and r are scattering amplitudes entering matrix Eq. (1), ϕ_0 is determined by the relation

$$\cos(2\pi\phi_0) = \cos\theta\cos(2\pi\phi), \tag{16}$$

and the matrix $\hat{H}$ is given by

$$\hat{H} = \begin{pmatrix} a & be^{i\xi} \\ be^{-i\xi} & -a \end{pmatrix}, \tag{17}$$

where ξ is defined in Eq. (4). The coefficients

$$a = i\,\frac{e^{-2\pi i\phi} - \cos(2\pi\phi_0)\cos\theta}{\cos\theta\sin(2\pi\phi_0)}, \tag{18}$$

$$b = \frac{e^{-2\pi i\phi}\tan\theta}{\sin(2\pi\phi_0)}, \tag{19}$$

are related by the relation $a^2 + b^2 = 1$.

Calculations shows that asymmetry of the arms does not play any role in the HI. Also, position of BD x_0 drops out from final expressions for $\mathscr{T}$ and $\mathscr{F}$. We therefore consider two cases: identical contacts (see next subsection and App. A) and non-identical contacts (see App. B)

Generalization of Eq. (15) for the case of different tunneling contacts characterized by amplitudes t_L and t_R is straightforward. One should make in this equation the following replacement:

$$t \to \sqrt{t_L t_R}, \quad r \to \sqrt{r_L r_R}, \quad \xi \to \xi + i\beta,$$

where the parameter describing the difference of tunneling contacts (see also App. B) is

$$\beta = \frac{1}{2}\ln(t_R/t_L)\,. \tag{20}$$

3.3. Results (identical contacts)

The transmission coefficient and the Fano factor are obtained with the use of Eqs. (7), (11), (12),N(13), and (**??**). Direct energy averaging in Eqs. (11) and (12) yields [34]

$$\mathscr{T} = \tanh\lambda\left[1 - \frac{\sin^2\theta\sinh^2\lambda\cosh(2\lambda)}{\cosh^2(2\lambda) - \cos^2\theta\cos^2(2\pi\phi)}\right] \tag{21}$$

and [52]

$$\mathscr{T}_2 = \tilde{C}\sum_{m,n=0}^{3}\tilde{A}_{(m,n)}\frac{\sinh^{2n}\lambda}{D^m}\,. \tag{22}$$

Here

$$D = \sinh^2(2\lambda) + R_\theta + (1 - R_\theta)R_\phi\,,$$

$$\tilde{C} = \tanh\lambda/\cosh^2\lambda, \quad R_\theta = \sin^2\theta, \quad R_\phi = \sin^2(2\pi\phi). \tag{23}$$

The coefficients $\tilde{A}_{(m,n)}$ depend on R_θ, R_ϕ but do not depend on λ. Analytical expressions for these coefficients are presented in the App. A. The Fano factor is connected with $\mathscr{T}$ and $\mathscr{T}_2$ by Eq. (13).

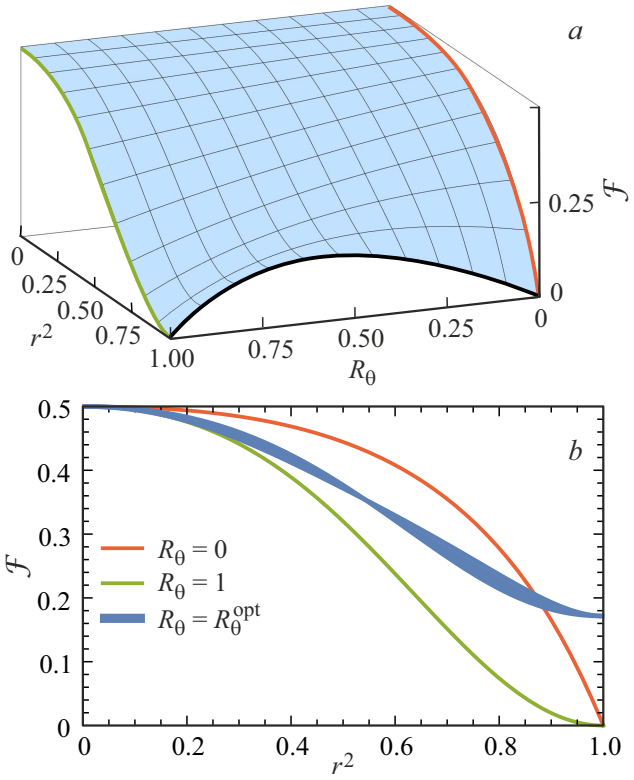

Figure 3. Panel (a): The dependence of the Fano factor, $\mathscr{F}$, on r^2 and the strength of the magnetic impurity, R_θ; for $r \to 1$ there an is optimal value, $R_\theta = R_\theta^{\rm opt}$, where the Fano factor has maximum. Panel (b): Cross-sections of panel (a) at different values of R_θ; dependence on the flux is weak and is illustrated for $R_\theta = R_\theta^{\rm opt}$ by broadening of the curve (shown by blue color) for flux belonging to interval $0 < \phi < 1$ (these figures were presented in Ref. [52] in a slightly different way). The point $r = 1$ is „noiseless“ both for ballistic case $R_\theta = 0$ and the case of very strong defect $R_\theta = 1$.

In Figure 3, a, we present dependence of the Fano factor, on r^2 and the strength of the magnetic impurity, R_θ for $\phi = 0$. One can see that for „metallic“ contact, $r \to 1$, dependence on the backscattering strength R_θ is non-monotonous.

In Figure 3, b, we plot dependence of $\mathscr{F}$ on r^2 for fixed R_θ. Two limiting dependencies, corresponding to absence of impurity, $R_\theta = 0$, and very strong impurity, $R_\theta = 1$, are shown by orange and green line, respectively. In both cases, there is no dependence on the magnetic flux. For any other R_θ in the interval $0 < R_\theta < 1$, the Fano factor depends on ϕ. Each curve corresponding to certain R_θ broadens as illustrated by blue curve corresponding to $R_\theta = R_\theta^{\rm opt}$.

In order to emphasize this dependence one can consider normalized value

$$\mathscr{F}_n(\phi) = \frac{\mathscr{F}(\phi) - \mathscr{F}(1/4)}{\mathscr{F}(0) - \mathscr{F}(1/4)}. \tag{24}$$

The dependence of the normalized quantity $\mathscr{F}_n$ on the magnetic flux for several sets of parameters R_θ and λ is

shown in Figure 4 along with the flux dependence of the normalized transmission coefficient. One can see sharp resonances both in $\mathscr{F}_n$ and $\mathscr{T}_n$ at weak tunneling coupling and small R_θ (see Figure 4, *c*) which evolve into harmonic Aharonov–Bohm oscillations with increasing λ and R_θ (see Figure 4, *d*).

One can present results of the calculation as a family of curves $\mathscr{F}(\mathscr{T})$ plotted for fixed ϕ and different (but also fixed) R_θ, see Figure 5. This fugure is one of the our key results. Indeed, measuring simultaneously both conductance and noise and using Figure 5), one can find the strength of the backscattering defect, R_θ. It is worth stressing that measuring the conductance only is insufficient to find the strength of the defect, because the conductance depends also on the properties of the contacts, which are actually not known to a sufficient precision. Importantly, by using both conductance and noise measurements, together with Figure 5 we can find R_θ without having any information about amplitudes t and r, characterizing the contacts. It can help to identify backscattering mechanism that apparently always exists in the realistic experimental structures [4].

3.4. Limiting cases

Here, we discuss several limiting cases allowing for simple analytical description.

In the absence of a magnetic defect, $R_\theta = 0$, interference effects are absent as we discussed in the introduction, so that expressions for the Fano factor and transmission coefficient dramatically simplify:

$$\mathscr{T} = \tanh[\lambda], \quad \mathscr{F} = \frac{1}{2\cosh^2[\lambda]}. \tag{25}$$

These equations do not depend on ϕ and are related by the same equation as for ballistic SCI

$$\mathscr{F} = \frac{1}{2}\left[1 - \mathscr{T}^2\right] \tag{26}$$

(see Eq. (20) in Ref. [53]). This dependence is shown in Figure 5 by red line

The formulas for the conductance and Fano factor in case of different tunneling contacts can also be obtained in closed form and are presented in App. B. An analog of Eq. (26) in case of different tunneling contacts reads

$$\mathscr{F} = \left[1 - \mathscr{T}^2\right] \times \sqrt{\sinh^2(2\beta) + \mathscr{T}^2} \Big/ \left(\sqrt{\sinh^2(2\beta) + \mathscr{T}^2} + \mathscr{T}\cosh(2\beta)\right), \tag{27}$$

with the asymmetry parameter β given by Eq. (20). This equation is similar but a bit more cumbersome than analogous equation for SCI (see Eq. (28) in Ref. [53]).

The Fano factor and transmission coefficient also do not depend on the magnetic flux for the strong magnetic impurity, $R_\theta = 1$ (green curves on the Figure 3, accordingly). In this case, we have

$$\mathscr{T} = \frac{1}{2}\tanh[2\lambda], \quad \mathscr{F} = \frac{1}{2\cosh^2[2\lambda]}, \tag{28}$$

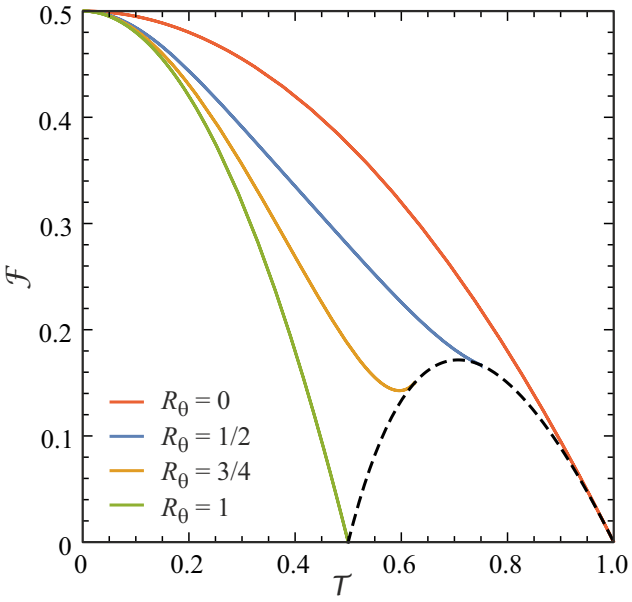

Figure 5. The combined dependence of Fano factor, $\mathscr{F}$, and the transmission coefficient, $\mathscr{T}$, on the transparency of the contact, λ, for different strength of the magnetic impurity, R_θ, and the magnetic flux $\phi = 0.4$, according to Eqs. (21), (22). The black dashed line borders the area of maximum transmission coefficient for given R_θ.

$$\mathscr{F} = \frac{1}{2} - 2\mathscr{T}^2. \tag{29}$$

Last dependence is shown by green line in Figure 5.

The flux dependence is also absent for the open interferometer, $r = 1$ ($\lambda = \infty$). In this case, we get

$$\mathscr{T} = 1 - \frac{R_\theta}{2},$$

$$\mathscr{F} = R_\theta \frac{1 - R_\theta}{2 - R_\theta} = \frac{(2\mathscr{T} - 1)(1 - \mathscr{T})}{\mathscr{T}}. \tag{30}$$

Hence, the Fano factor has a maximum as a function of backscattering probability as is shown by the black curve in the Figure 3, *a*.

Equation (30) has a simple physical meaning. For $r = 1$, the windings are absent, and there are two parallel conductors, i. e. lower and upper arms of the HI. The lower arm, with spin $\downarrow$, is an ideal conductor with the transmission coefficient $\mathscr{T}_\downarrow = 1$ while the transmission through the upper arm is controlled by the magnetic defect, $\mathscr{T}_\uparrow = \cos^2\theta$, varying from 0 to 1. Then, we get

$$\mathscr{F} = \frac{\mathscr{T}_\uparrow(-\mathscr{T}_\uparrow)}{1 + \mathscr{T}_\uparrow}. \tag{31}$$

Taking into account that the total transmission coefficient in this case is given by $\mathscr{T} = (\mathscr{T}_\uparrow + 1)/2$, we arrive to Eq. (30). We have maximum $\mathscr{F}_{\max} = 3 - 2\sqrt{2} \approx 0.17$ at $\mathscr{T}_{\uparrow,\max} = \sqrt{2} - 1$ and, respectively, $R_\theta^{\max} = 2 - \sqrt{2} \approx 0.59$. The total transmission coefficient at this point is given by

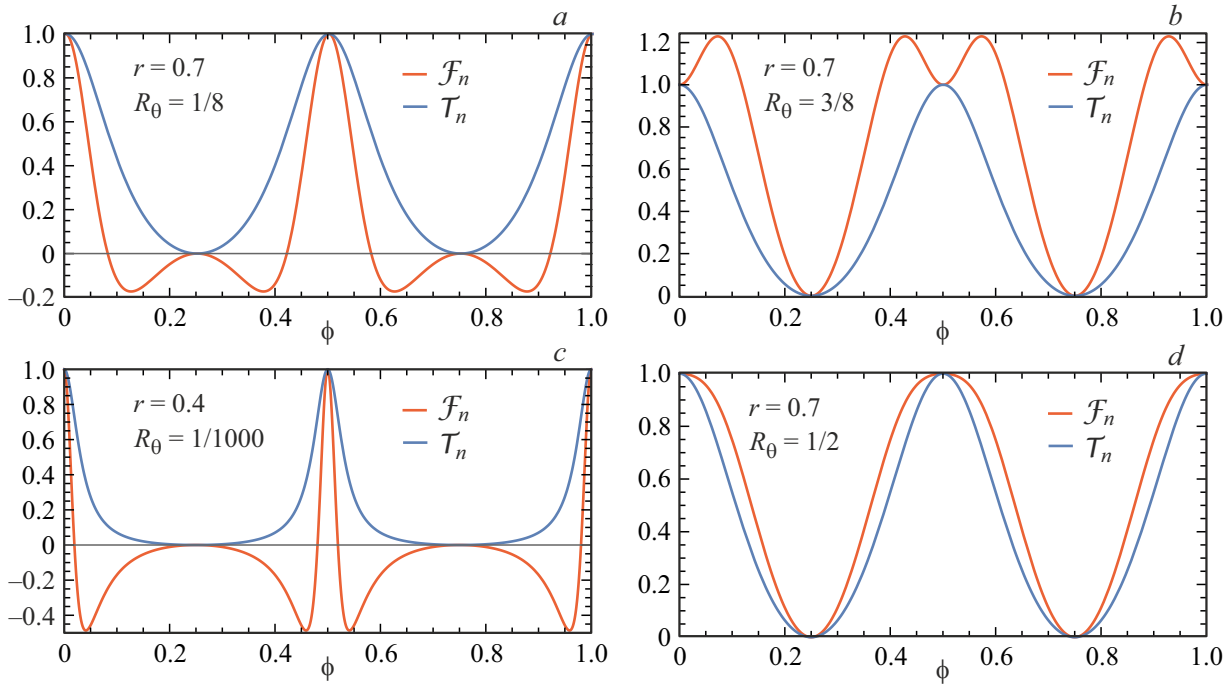

Figure 4. Dependence of the normalized factor Fano, $\mathscr{F}_n$, and the normalized conductance, $\mathscr{T}_n$, for the helical interferometer on magnetic flux, ϕ, at different strengths of scattering by a magnetic defect R_θ and tunneling amplitude, r. (a) $r = 0.7$, $R_\theta = 1/8$; (b) $r = 0.7$, $R_\theta = 3/8$; (c) $r = 0.4$, $R_\theta = 1/1000$; (d) $r = 0.7$, $R_\theta = 1/2$. Shape of the curve $\mathscr{F}(\phi)$ strongly depends on the transparency of the contacts.

$\mathscr{T}_{\max} = 1/\sqrt{2}$. We notice that Eq. (30) describes both black line in Figure 3, a and dashed black line in Figure 5.

In order to combine here analytical formulas for all relevant cases, we also present at the end of this section several equations obtained previously in Ref. [52]. For almost metallic contact, $t \ll 1$ ($\lambda \to \infty$), and for an arbitrary scattering strength on a magnetic defect, $\mathscr{T}$ shows weak oscillations with ϕ:

$$\mathscr{T} \approx \frac{R_\theta(1-R_\theta)}{2-R_\theta} + 2t^2 + 2t^4 \frac{R_\theta(1-R_\theta)\left(10-12R_\theta+3R_\theta^2\right)}{(2-R_\theta)^2}\cos(4\pi\phi). \quad (32)$$

More interesting is the opposite case of an almost tunnel contact: $t \to 1$, $r = \sqrt{1-t^2} \ll \theta$. In this case,

$$\mathscr{T} \approx \frac{1}{2} - \frac{r^4}{8}\left[1 + \frac{3R_\theta}{R_\phi + R_\theta - R_\theta R_\phi}\right]. \quad (33)$$

This formula shows weak but sharp resonances with magnetic flux. These resonances are well pronounced in the normalized Fano factor. Indeed, from Eqs. (24) and (33) for $\theta \ll 1$ we obtain

$$\mathscr{F}_n \approx \frac{\theta^2}{\theta^2 + \sin^2(2\pi\phi)},$$

i. e. sharp resonances at $\phi = 0$ and $\phi = 1/2$.

4. Comparison of single-channel and helical interferometers

Recently, we studied the shot noise in single-channel interferometers [53]. Let us briefly compare SCI and HI. Interestingly, these interferometers, while having similar ring geometry and a number of similar properties, exhibit fundamentally different physical behavior in a number of respects, due to their different electronic structures.

Let us discuss the similarities and differences between these interferometers in more detail. It was shown that the shot noise in both systems is substantially modified by quantum interference effects. It is essential that the interference effects survive in the high temperature limit, $T \gg \Delta$. The appearance of temperature-robust interference effects stems from trajectories interfering at any energy. In case of symmetric SCI for any trajectory entering the interferometer and moving clockwise there is another trajectory moving counterclockwise, and these trajectories interfere destructively at $\phi = 1/2$. Such destructive interference is exact, i. e. the transmission amplitude is identically zero at all energies, $t(\varepsilon, \phi = 1/2) \equiv 0$ [24] (see also the discussion of the consequences of this identity in [27,30]). The peculiarity of interference effects in HI lies in the fact that they appear only in presence of backscattering defects. In this case trajectories interfering at any energy appear as well, namely, trajectories returning to the defect after n revolutions clockwise and counterclockwise are always interfering. The relative phase of such trajectories is $4\pi n\phi$,

Table 1. Comparison of key characteristics

Feature	Conventional Single-Channel Spinless Interferometer	Helical Interferometer
AB oscillation period	$\Delta\phi = 1$	$\Delta\phi = 1/2$
Ballistic interference	Yes	No
Flux dependence strength	Strong	Weak
Contact sensitivity	High	Low
Geometric asymmetry	Strong effect	No effect

and as a result the Aharonov–Bohm oscillation period (both in $\mathscr{T}$ and in $\mathscr{F}$) in HI equals to $\Delta\phi = 1/2$, in contrast to SCI, where the oscillation period is equal to $\Delta\phi = 1$.

One of the conclusions following from our calculations is that the interference effects are less pronounced for HI and, consequently, the influence of the magnetic field on the Fano factor is weaker as compared to SCI. The reason is that the interference comes into play for SCI already in the ballistic case, when impurities in the arms of SCI are absent (see discussion in Ref. [53]), while the Aharonov–Bohm peaks in HI are proportional to the backscattering probability. On the other hand, interference effects in HI although being weaker are more robust to variation of geometry and contact properties. In particular, asymmetrical placements of contacts results in strong modification of noise Fano factor in SCI [53] in contrast to HI. Specifically, the asymmetry of the SCI strongly affects the noise intensity even for fixed magnetic flux, so that changing difference of shoulder's lengths, $L_1 - L_2$, within a small interval about the Fermi wavelength, one changes $\mathscr{F}_{\mathrm{SCI}}$ by a factor on the order of unity (see Figure 5 in Ref. [53]). By contrast, all analytical expressions for Fano factor and conductance of the HI contains total length of the edge $L_1 + L_2$ and do not depend on $L_1 - L_2$. We also find that the characteristics of the contact between the SCI and the leads strongly modify the noise in this case, even in the ballistic regime inside the SCI. In turn, the noise in case of HI is strongly impacted by the backscattering defects inside the HI ring.

We demonstrate that the simultaneous measurement of conductance and Fano factor in HI allows one to determine the strength of backscattering defects that violate topological protection in the realistic setups. As for SCI, it can show different noise for the same transmission coefficient (see, for example, Figure 6 in Ref. [53]). Hence, measuring, complementary to conductance, also the Fano factor of SCI would help to experimentally determine the type of the contacts to leads (see Figure 3, *a* and Figure 3, *b* in Ref. [53]) and the strength of tunneling coupling.

Features of both types of interferometers are summarized in Table 1.

5. Conclusion

We have developed a comprehensive theory of shot noise in helical Aharonov–Bohm interferometers, revealing how noise measurements can probe the breakdown of topological protection in 2D topological insulators. Our analysis demonstrates that quantum interference effects in helical edge states produce distinctive signatures in current noise that provide crucial information about backscattering mechanisms.

The central result of our work is that simultaneous measurement of conductance and Fano factor enables direct determination of backscattering strength, without requiring any detailed knowledge of contact properties. This is particularly valuable given that contacts in real devices are often poorly characterized. The parametric relationship between $\mathscr{F}$ and $\mathscr{T}$ (Figure 5) provides an experimental roadmap for quantifying backscattering probabilities. Specifically, measuring one point on this picture allows us to unambiguously find the strength of the defect R_θ

We have shown that helical interferometers exhibit AB oscillations of both conductance and the Fano factor with the period $\Delta\phi = 1/2$, distinct from the $\Delta\phi = 1$ period in SCI. This halved periodicity arises from the spin-momentum locking in helical edge states and serves as a clear experimental signature. The oscillation amplitude is directly proportional to the backscattering probability, making noise measurements a sensitive probe of topological protection violation.

An important finding concerns the different behavior for ballistic ($R_\theta = 0$) and strongly backscattering ($R_\theta = 1$) limits. In both cases, the Fano factor becomes flux-independent, while intermediate backscattering strengths show although weak but characteristic flux dependence. This provides a way to distinguish between different scattering regimes.

Our treatment of non-identical contacts addresses the experimental reality of asymmetric device fabrication. The analytical expressions we provide allow extraction of backscattering parameters even when contact transparencies differ significantly. This practical consideration enhances the experimental relevance of our predictions.

From an experimental perspective, recent advances in fabricating quantum point contacts to helical edge states [48] make our predictions directly testable. The high-temperature regime $T \gg \Delta$ corresponds to experimentally accessible conditions (typically a few Kelvin for micron-scale devices), and the predicted relationships between conductance and noise provide clear experimental benchmarks.

In summary, shot noise measurements in helical interferometers offer a powerful diagnostic tool for quantifying

the breakdown of topological protection in real materials. By providing complementary information to conductance measurements, noise characterization can help identify the microscopic mechanisms responsible for backscattering — whether magnetic impurities, bulk disorder, or other effects — thus advancing our understanding of topological phases in realistic experimental settings.

Funding

The work was carried out with financial support from the Russian Science Foundation (grant No. 25-12-00212), https://rscf.ru/project/25-12-00212/.

Conflict of interest

The authors of this work declare that they have no conflicts of interest.

A. Identical contacts

General formulas for the conductance and the noise intensity are obtained by averaging the expressions (6), (7), (8) and (9) in the main text over the energy, using expressions for the amplitude (15). This result was obtained early in Ref. [52] in different form. It is convenient to write the resulting formulas, using the parameters λ, R_θ and R_ϕ instead of the parameters t, θ and ϕ, according to the following definitions:

$$t = e^{-\lambda}, \quad r = \sqrt{1 - e^{-2\lambda}}, \quad 0 < \lambda < \infty, \tag{34}$$

$$R_\theta = \sin^2\theta, \tag{35}$$

$$R_\phi = \sin^2(2\pi\phi). \tag{36}$$

Direct calculation of energy averages in formulas (11) and (12) yields

$$\mathscr{T} = C \sum_{m,n=0}^{1} A_{(m,n)} \frac{\sinh^{2n}\lambda}{D^m}, \tag{37}$$

$$\mathscr{T}_2 = \tilde{C} \sum_{m,n=0}^{3} \tilde{A}_{(m,n)} \frac{\sinh^{2n}\lambda}{D^m}, \tag{38}$$

with

$$\begin{aligned}
D &= \sinh^2(2\lambda) + R_\theta + (1 - R_\theta)R_\phi, \\
C &= \tanh\lambda, \\
A_{(0,0)} &= 1 - R_\theta/2, \\
A_{(0,1)} &= 0, \\
A_{(1,0)} &= R_\theta\big(R_\theta + (1 - R_\theta)R_\phi\big)/2, \\
A_{(1,1)} &= R_\theta,
\end{aligned} \tag{39}$$

which leads to Eq. (21) and

$$\begin{aligned}
\tilde{C} &= \tanh\lambda/\cosh^2\lambda, \\
\tilde{A}_{(0,0)} &= 1 + R_\theta(1 - R_\theta/2), \\
\tilde{A}_{(0,1)} &= 2 - R_\theta(2 - R_\theta), \\
\tilde{A}_{(1,0)} &= R_\theta^2\big(R_\theta + R_\phi(1 - R_\theta)\big)/4, \\
\tilde{A}_{(1,1)} &= R_\theta(R_\theta - 4(1 - R_\theta)(3 - 2R_\theta)(1 - R_\phi))/2, \\
\tilde{A}_{(2,0)} &= -R_\theta(2 - R_\theta)\big(R_\theta + R_\phi(1 - R_\theta)\big)^2/2, \\
\tilde{A}_{(2,1)} &= -R_\theta\big(R_\theta(1 - R_\phi) + R_\phi\big) \\
&\quad \times \big(R_\theta(13 - 9R_\theta(1 - R_\phi) - 17R_\phi) + 8R_\phi\big)/2, \\
\tilde{A}_{(2,2)} &= -R_\theta\big(R_\theta(9 - 7R_\theta(1 - R_\phi) - 11R_\phi) + 4R_\phi\big), \\
\tilde{A}_{(3,0)} &= -R_\theta^2\big(R_\theta + R_\phi(1 - R_\theta)\big)^3/4, \\
\tilde{A}_{(3,1)} &= -3R_\theta^2\big(R_\theta + R_\phi(1 - R_\theta)\big)^3/2, \\
\tilde{A}_{(3,2)} &= -3R_\theta^2\big(R_\theta + R_\phi(1 - R_\theta)\big)^2, \\
\tilde{A}_{(3,3)} &= -R_\theta^2\big(4 - 2R_\theta(1 - R_\phi) - 2R_\phi\big)\big(R_\theta(1 - R_\phi) + R_\phi\big), \\
\tilde{A}_{(0,2)} &= \tilde{A}_{(0,3)} = \tilde{A}_{(1,2)} = \tilde{A}_{(1,3)} = \tilde{A}_{(2,3)} = 0.
\end{aligned} \tag{40}$$

B. Non-identical contacts

In general case the tunneling rates in different contacts of the interferometer are described by unequal tunneling amplitudes

$$\begin{aligned}
t_{R,L} &= te^{\pm\beta}, \quad |\beta| \le \lambda \\
t_R t_L &= e^{-2\lambda}, \\
t_R/t_L &= e^{2\beta}.
\end{aligned} \tag{41}$$

In this case we may still use the expressions (37), (22), but the coefficients should be redefined, $A_{(m,n)} \to A^{\mathrm{u}}_{(m,n)}$, $\tilde{A}_{(m,n)} \to \tilde{A}^{\mathrm{u}}_{(m,n)}$, as follows

$$\begin{aligned}
C^{\mathrm{u}} &= C\left(1 - \frac{\sinh^2\beta}{\sinh^2\lambda}\right), \\
A^{\mathrm{u}}_{(0,0)} &= A_{(0,0)}, \\
A^{\mathrm{u}}_{(0,1)} &= 0, \\
A^{\mathrm{u}}_{(1,0)} &= A_{(1,0)} + R_\theta \sinh^2\beta, \\
A^{\mathrm{u}}_{(1,1)} &= A_{(1,1)} + 2R_\theta \sinh^2\beta, \\
\tilde{C}^{\mathrm{u}} &= \tilde{C}\left(1 - \frac{\sinh^2\beta}{\sinh^2\lambda}\right)^2, \\
\tilde{A}^{\mathrm{u}}_{(0,0)} &= \tilde{A}_{(0,0)} + 2R_\theta(2 - R_\theta)\sinh^2\beta, \\
\tilde{A}^{\mathrm{u}}_{(0,1)} &= \tilde{A}_{(0,1)},
\end{aligned}$$

$$
\begin{aligned}
\tilde{A}^{\mathrm{u}}_{(1,0)} &= \tilde{A}_{(1,0)} + R_\theta(12 - R_\theta(17 - 9R_\theta) \\
&\quad - 3(1-R_\theta)(4-3R_\theta)R_\phi + 4R_\theta \sinh^2\beta)\sinh^2\beta/2\,, \\
\tilde{A}^{\mathrm{u}}_{(1,1)} &= \tilde{A}_{(1,1)} + R_\theta^2 \sinh^2(2\beta)\,, \\
\tilde{A}^{\mathrm{u}}_{(2,0)} &= \tilde{A}_{(2,0)} + R_\theta(R_\theta(1-R_\phi) + R_\phi) \\
&\quad \times (R_\theta(13 - 7R_\theta(1-R_\phi) - 11R_\phi) \\
&\quad - 4(2-R_\phi))\sinh^2\beta/2 + 5R_\theta^2(1-R_\theta)(1-R_\phi)\sinh^4\beta\,, \\
\tilde{A}^{\mathrm{u}}_{(2,1)} &= \tilde{A}_{(2,1)} - 4R_\theta(2-R_\theta)(R_\theta(1-R_\phi) + R_\phi)\sinh^2\beta \\
&\quad + 10R_\theta^2(1-R_\theta)(1-R_\phi)\sinh^4\beta\,, \\
\tilde{A}^{\mathrm{u}}_{(2,2)} &= \tilde{A}_{(2,2)} - 2R_\theta(R_\theta(9 - 7R_\theta(1-R_\phi) - 11R_\phi) \\
&\quad + 4R_\phi)\sinh^2\beta\,, \\
\tilde{A}^{\mathrm{u}}_{(3,0)} &= \tilde{A}_{(3,0)} - R_\theta^2(R_\theta(1-R_\phi) + R_\phi) \\
&\quad \times ((R_\theta(1-R_\phi) + R_\phi)(2 - R_\theta(1-R_\phi) - R_\phi) \\
&\quad + (4 - 3R_\theta(1-R_\phi) - 3R_\phi)\sinh^2\beta)\sinh^2\beta\,, \\
\tilde{A}^{\mathrm{u}}_{(3,1)} &= \tilde{A}_{(3,1)} - 6R_\theta^2(R_\theta(1-R_\phi) + R_\phi)(R_\theta(1-R_\phi) + R_\phi \\
&\quad + (2 - R_\theta(1-R_\phi) - R_\phi)\sinh^2\beta)\sinh^2\beta\,, \\
\tilde{A}^{\mathrm{u}}_{(3,2)} &= \tilde{A}_{(3,2)} - 12R_\theta^2(R_\theta(1-R_\phi) + R_\phi)(R_\theta(1-R_\phi) \\
&\quad + R_\phi + \sinh^2\beta)\sinh^2\beta\,, \\
\tilde{A}^{\mathrm{u}}_{(3,3)} &= \tilde{A}_{(3,3)} - 2R_\theta^2(R_\theta(1-R_\phi) + R_\phi)\sinh^2(2\beta)\,, \\
\tilde{A}^{\mathrm{u}}_{(0,2)} &= \tilde{A}^{\mathrm{u}}_{(0,3)} = \tilde{A}^{\mathrm{u}}_{(1,2)} = \tilde{A}^{\mathrm{u}}_{(1,3)} = \tilde{A}^{\mathrm{u}}_{(2,3)} = 0\,.
\end{aligned}
\tag{42}
$$

References

[1] M.Z. Hasan, C.L. Kane. Rev. Mod. Phys., **82** (4), 3045 (2010).
[2] X.-L. Qi, S.-C. Zhang. Rev. Mod. Phys., **83** (4), 1057 (2011).
[3] B. Bernevig, T. Hughes. *Topological Insulators and Topological Superconductors*, (Princeton University Press, Princeton, 2013).
[4] E. Olshanetsky, Z. Kvon, G. Gusev, N. Mikhailov. Physica E, **147**, 115605 (2023).
[5] M.J.M. de Jong, C.W.J. Beenakker. *Mesoscopic Electron Transport*, L. Sohn, L. Kouwenhoven, ed by G. Schön, 345 *NATO ASI Series E*, 225–258, (Kluwer Academic Publishing, Dordrecht, 1997).
[6] Y. Blanter, M. Büttiker. Phys. Rep., **336** (1-2), 1 (2000).
[7] N. Lezmy, Y. Oreg, M. Berkooz. Phys. Rev. B, **85** (23), 235304 (2012).
[8] A. Del Maestro, T. Hyart, B. Rosenow. Phys. Rev. B, **87** (16), 165440 (2013).
[9] E.S. Tikhonov, D.V. Shovkun, V.S. Khrapai, Z.D. Kvon, N.N. Mikhailov, S.A. Dvoretsky. JETP Lett., **101** (10), 708 (2015).
[10] A. Mani, C. Benjamin. Sci. Rep., **7** (1) (2017).
[11] J.I. Väyrynen, L.I. Glazman. Phys. Rev. Lett., **118** (10), 106802 (2017).
[12] S.U. Piatrusha, L.V. Ginzburg, E.S. Tikhonov, D.V. Shovkun, G. Koblmüller, A.V. Bubis, A.K. Grebenko, A.G. Nasibulin, V.S. Khrapai. JETP Lett., **108** (1), 71 (2018).
[13] P.D. Kurilovich, V.D. Kurilovich, I.S. Burmistrov, Y. Gefen, M. Goldstein. Phys. Rev. Lett., **123** (5), 056803 (2019).
[14] V.D. Kurilovich, P.D. Kurilovich, I.S. Burmistrov, M. Goldstein. Phys. Rev. B, **99**, 085407 (2019).
[15] B.V. Pashinsky, M. Goldstein, I.S. Burmistrov. Phys. Rev. B, **102** (12), 125309 (2020).
[16] C.-H. Hsu, P. Stano, J. Klinovaja, D. Loss. Semicond. Sci. Tech., **36** (12), 123003 (2021).
[17] B. Probst, P. Virtanen, P. Recher. Phys. Rev. B, **106** (8), 085406 (2022).
[18] S. Mishra, C. Benjamin. Phys. Rev. B, **108** (11), 115301 (2023).
[19] J.I. Väyrynen, M. Goldstein, L.I. Glazman. Phys. Rev. Lett., **110** (21), 216402 (2013).
[20] P.P. Aseev, K.E. Nagaev. Phys. Rev. B, **94** (4), 045425 (2016).
[21] I.V. Krainov, R.A. Niyazov, D.N. Aristov, V.Y. Kachorovskii. **122** (8), 495 (2025).
[22] Y. Aharonov, D. Bohm. Phys. Rev., **115** (3), 485 (1959).
[23] Y. Aharonov, D. Bohm. Phys. Rev., **130** (4), 1625 (1963).
[24] M. Büttiker, Y. Imry, M.Y. Azbel. Phys. Rev. A, **30** (4), 1982 (1984).
[25] M. Büttiker, Y. Imry, R. Landauer, S. Pinhas. Phys. Rev. B, **31** (10), 6207 (1985).
[26] E.A. Jagla, C.A. Balseiro. Phys. Rev. Lett., **70** (5), 639 (1993).
[27] A.P. Dmitriev, I.V. Gornyi, V.Y. Kachorovskii, D.G. Polyakov. Phys. Rev. Lett., **105** (3), 036402 (2010).
[28] P.M. Shmakov, A.P. Dmitriev, V.Y. Kachorovskii. Phys. Rev. B, **85** (7), 75422 (2012).
[29] P.M. Shmakov, A.P. Dmitriev, V.Y. Kachorovskii. Phys. Rev. B, **87** (23), 235417 (2013).
[30] A.P. Dmitriev, I.V. Gornyi, V.Y. Kachorovskii, D.G. Polyakov, P.M. Shmakov. JETP Lett., **100** (12), 839 (2015).
[31] A.P. Dmitriev, I.V. Gornyi, V.Y. Kachorovskii, D.G. Polyakov. Phys. Rev. B, **96** (11), 115417 (2017).
[32] R.A. Niyazov, D.N. Aristov, V.Y. Kachorovskii. Phys. Rev. B, **98** (4), 045418 (2018).
[33] R.A. Niyazov, D.N. Aristov, V.Y. Kachorovskii. npj Comput. Mater., **6** (1) (2020).
[34] R.A. Niyazov, D.N. Aristov, V.Y. Kachorovskii. Phys. Rev. B, **103** (12), 125428 (2021).
[35] R.A. Niyazov, D.N. Aristov, V.Y. Kachorovskii. JETP Lett., **113** (11), 689 (2021).
[36] R.A. Niyazov, D.N. Aristov, V.Y. Kachorovskii. Phys. Rev. B, **108** (7), 075424 (2023).
[37] D.E. Feldman, Y. Gefen, A. Kitaev, K.T. Law, A. Stern. Phys. Rev. B, **76** (8), 085333 (2007).
[38] C. Wang, D.E. Feldman. Phys. Rev. B, **82** (16), 165314 (2010).
[39] G. Yang. Phys. Rev. B, **91** (11), 115109 (2015).
[40] K. Kobayashi, M. Hashisaka. J. Phys. Soc. Jpn., **90** (10), 102001 (2021).
[41] J.M. Edge, J. Li, P. Delplace, M. Büttiker. Phys. Rev. Lett., **110** (24), 246601 (2013).
[42] F. Dolcini. Phys. Rev. B, **92** (15), 155421 (2015).
[43] H.R. Shea, R. Martel, P. Avouris. Phys. Rev. Lett., **84** (19), 4441 (2000).
[44] V. Piazza, F. Beltram, W. Wegscheider, C.-T. Liang, M. Pepper. Phys. Rev. B, **62** (16), R10630 (2000).
[45] A. Fuhrer, S. Lüscher, T. Ihn, T. Heinzel, K. Ensslin, W. Wegscheider, M. Bichler. Nature, **413** (6858), 822 (2001).

[46] U.F. Keyser, C. Fühner, S. Borck, R.J. Haug, M. Bichler, G. Abstreiter, W. Wegscheider. Phys. Rev. Lett., **90** (19), 196601 (2003).
[47] S. Zou, D. Maspoch, Wang, C.A. Mirkin, G.C. Schatz. Nano Lett., **7** (2), 276 (2007).
[48] S. Munyan, A. Rashidi, A.C. Lygo, R. Kealhofer, S. Stemmer. Nano Lett., **23** (12), 5648 (2023).
[49] L. Du, I. Knez, G. Sullivan, R.-R. Du. Phys. Rev. Lett., **114** (9), 96802 (2015).
[50] S.-B. Zhang, Y.-Y. Zhang, S.-Q. Shen. Phys. Rev. B, **90** (11), 115305 (2014).
[51] L.-H. Hu, D.-H. Xu, F.-C. Zhang, Y. Zhou. Phys. Rev. B, **94** (8), 85306 (2016).
[52] R.A. Niyazov, I.V. Krainov, D.N. Aristov, V.Y. Kachorovskii. JETP Lett., **119** (5), 372 (2024).
[53] R.A. Niyazov, I.V. Krainov, D.N. Aristov, V.Y. Kachorovskii. Semiconductors, **59** (8), 430 (2025).
[54] K.E. Nagaev, S.V. Remizov, D.S. Shapiro. JETP Lett., **108** (10), 664–669 (2018).
[55] D.V. Khomitsky, A.A. Konakov, E.A. Lavrukhina. J. Phys. Condens. Matter, **34** (40), 405302 (2022).
[56] V.A. Sablikov, A.A. Sukhanov. Phys. Rev. B, **103** (15), 155424 (2021).